Extended Bose-Hubbard model with dipolar and contact interactions

Krzysztof Biedroń,[1] Mateusz Łącki,[1] and Jakub Zakrzewski[1,2]
[1]*Instytut Fizyki imienia Mariana Smoluchowskiego, Uniwersytet Jagielloński, Łojasiewicza 11, 30-048 Kraków, Poland*
[2]*Mark Kac Complex Systems Research Center, Jagiellonian University, Łojasiewicza 11, 30-348 Kraków, Poland*

(Received 2 March 2018; revised manuscript received 23 May 2018; published 5 June 2018)

We study the phase diagram of the one-dimensional boson gas trapped inside an optical lattice with contact and dipolar interaction, taking into account next-nearest terms for both tunneling and interaction. Using the density-matrix renormalization group, we calculate how the locations of phase transitions change with increasing dipolar interaction strength for average density $\rho = 1$. Furthermore, we show the emergence of pair-correlated phases for a large dipolar interaction strength and $\rho \geqslant 2$, including a supersolid phase with an incommensurate density wave ordering manifesting the corresponding spontaneous breaking of the translational symmetry.

DOI: 10.1103/PhysRevB.97.245102

I. INTRODUCTION

Ultracold gases loaded in optical lattices enable simulation of a broad range of lattice gas models, most prominently the Bose-Hubbard (BH) model [1] with Mott insulator (MI) to superfluid (SF) quantum phase transition [2]. Precise control of model parameters is achieved by optical potential manipulation or by advanced techniques such as Feshbach resonances [3,4]. Long-range dipolar interparticle interactions are often taken into account by adding a simple nearest-neighbor interaction term resulting in the extended Bose-Hubbard (EBH) model, which has been the topic of numerous theoretical [5–16] and experimental [17] works.

A feature of ultracold gases is the ability to control the geometry of the underlying optical lattice potential or even the possibility of implementation of a more complex unit cell. The boundary conditions of the potentials can be set by an external harmonic or a box trap, leading to the open boundary conditions (OBCs) [18,19], or by arranging a system into a ringlike or cylinderlike geometry [20,21], thus implementing periodic boundary conditions (PBCs). Notably, one-dimensional systems offer the possibility of efficient many-body numerical simulations of the resulting lattice models by a family of methods related to the density-matrix renormalization group (DMRG) [22,23].

For one-dimensional lattices the EBH model features not only MI and SF phases but also an isolator density wave (DW) characterized by infinite-range spatial order, a topologically protected Haldane insulator (HI) with a nonzero value of the string order parameter, and supersolid (SS) phases which show both spatial ordering and superfluid behavior [24–26]. It has also been suggested that at the mean density $\rho = 3/2$ the EBH model features Fibonacci anyon excitations [27,28] corresponding to fractional domain walls between different DW phases. In this context, the mean-field analysis [27] predicted the existence of the SS phase between DW and SF phases, in contrast to the DMRG calculation [28].

The necessary strength of the dipole-dipole interactions is achieved for isotopes of dysprosium and erbium [29,30], Feshbach molecules [31], and polar molecules [32–34]. More exotic phases such as checkerboard and stripe-ordered phases are possible for higher-dimensional lattices [35–40] (for a review see [13]).

The BH and EBH models are motivated by an expansion of the field operators in the discrete basis defined by Wannier functions [1,41] for the optical potential, followed by truncating the physics to the lowest Bloch band and neglecting hopping beyond the nearest neighbors. The BH model includes only on-site interactions, while the EBH also contains density-density interactions on the nearest-neighbor sites. The rigor of this procedure has been the topic of extended research in the presence of fast-time dependence [42,43] and strong interatom interactions manifesting as so-called density-dependent tunnelings [13,32,44] and even as a renormalization of model parameters due to a virtual population of higher bands [45–47]. Moreover, the coupling beyond the nearest neighbor has been included in studies which treated shallow optical lattices [48,49] and for strongly interacting dipolar systems [50]. In the latter case the extra couplings led to the appearance of spatially ordered phases [35].

Extensive studies of the EBH-like models mentioned in this section were mostly done by scanning the parameter space of the constructed Hamiltonians at a chosen mean density or possibly under other constraints such as a ratio between parameters. In this study we take a more systematic approach to obtain the Hamiltonian for a dipolar gas of ultracold atoms in the optical lattice and study its phase diagram. First, our intent is to modify only experimentally accessible parameters such as the optical lattice potential depth, the scattering length for contact interactions, the dipole-dipole interaction strength, and the mean density of the gas. Second, we chose to keep all the relevant tight-binding terms describing tunneling and interactions. In this way the parameters of the obtained EBH-like Hamiltonians yield a realizable physical model. In other words we get natural constraint values of the parameters. This saves us from considering parameter ranges unaccessible experimentally. In the phase diagram defined by the experimentlike control knobs, we predict modifications of up-to-date theoretical results going beyond a simple readjustment of phase boundaries. In particular we provide evidence for the

emergence of a new phase: a pair superfluid phase with an incommensurate density wave order.

In Sec. II we derive the model from the microscopic principles identifying the realistic parameter set relevant for ultracold dipolar atoms and ultracold dipolar molecules. The phase diagrams for the system are presented in Sec. III (for the case of unit density in the lattice) and Sec. IV (for the case of other densities). In Sec. V we provide the final conclusions and outlook. We finish with three Appendixes describing in detail the computational methods used throughout the paper: in Appendix A we present our method of calculating the terms present in the Hamiltonian, Appendix B contains the parameters used in our DMRG runs, and in Appendix C we describe the DMRG method used in Sec. IV.

II. MODEL

The realistic Hamiltonian that models ultracold bosonic gas in the one-dimensional optical lattice potential considered in this work has the form

$$\begin{aligned} H =& -t\sum_{i=1}^{L-1}(b_i^\dagger b_{i+1}+\text{H.c.}) - t_{\text{nnn}}\sum_{i=1}^{L-2}(b_i^\dagger b_{i+2}+\text{H.c.}) \\ &+\frac{U}{2}\sum_{i=1}^{L} n_i(n_i-1) + V\sum_{i=1}^{L-1} n_i n_{i+1} + V_{\text{nnn}}\sum_{i=1}^{L-2} n_i n_{i+2} \\ &- T\sum_{i=1}^{L-1}[b_i^\dagger(n_i+n_{i+1})b_{i+1}+\text{H.c.}], \end{aligned} \tag{1}$$

where t, T, and V denote the amplitude for standard, nearest-neighbor tunnelings, the amplitude of density-dependent tunnelings resulting from interactions, and the strength of interactions between nearest-neighbor sites, respectively. The terms proportional to t_{nnn} and V_{nnn} are, respectively, the tunneling and strength of interaction between next-nearest-neighbor lattice sites.

The Hamiltonian (1) in its full glory is a result of a realistic tight-binding approximation to the many-body formulation continuous in space, as given by the second quantization. We consider an ultracold gas of atoms or molecules of mass m in the separable optical potential created by three pairs of standing waves of lasers with a wavelength λ_L which takes the form $V_{\text{opt}}(\mathbf{r}) = V_x\cos^2(k_L x) + V_y\cos^2(k_L y) + V_z\cos^2(k_L z)$, with $k_L = 2\pi/\lambda_L$. The recoil energy $E_R = \hbar^2 k_L^2/2m$ defines a natural energy scale for the single-particle physics. We take $V_y = V_z = 50E_R$ and $V_x \ll V_y, V_z$, which freezes the motion in directions y and z and leaves an effectively one-dimensional motion along the x axis. We can recover the parameters of (1) from (for more details see Appendix A)

$$\begin{aligned} H =& \int \psi^\dagger(r)\left[-\frac{\hbar^2\nabla^2}{2m} + V_{\text{opt}}(\mathbf{r})\right]\psi(r) \\ &+ \int \psi^\dagger(\mathbf{r})\psi^\dagger(\mathbf{r}')V(\mathbf{r}'-\mathbf{r})\psi(\mathbf{r}')\psi(\mathbf{r})d^3\mathbf{r}d^3\mathbf{r}'. \end{aligned} \tag{2}$$

The function $V(\mathbf{r})$ represents the sum of contact (V_c) and dipolar (V_d) interactions, $V(\mathbf{r}) = V_c(\mathbf{r}) + V_d(\mathbf{r})$, where

$$V_c(\mathbf{r}) = \frac{4\pi\hbar^2 a_s}{m}\delta(\mathbf{r}), \quad V_d(\mathbf{r}) = \frac{C_{dd}}{4\pi}\frac{1-3\cos^2\theta}{r^3}, \tag{3}$$

with θ being the angle between the direction of polarization and $\mathbf{r}$ and a_s being the scattering length for effective contact interactions [6].

The value of C_{dd} depends on the strength of dipolar interactions and has the form

$$C_{dd} = \begin{cases} \mu_0\mu_m^2, & \text{for magnetic dipole moment } \mu_m, \\ \mu_e^2/\epsilon_0, & \text{for electric dipole moment } \mu_e. \end{cases} \tag{4}$$

Later we will use a representation of the dipolar interaction strength by a dimensionless quantity:

$$d = \frac{mC_{dd}}{2\pi^3\hbar^2 a}. \tag{5}$$

In effect, we have two parameters, V_x and a_s, that can be controlled in the experiment (using the previously mentioned Feshbach resonance) and d, which depends on the kind of particles used in an experiment (we can, however, modify the strength of dipolar interactions by changing the direction of polarization). In the case of molecules, d can be controlled by the external electric field inducing the dipole moment. In this work, we set the dipole direction to be perpendicular to that of the lattice, so that dipolar interactions are maximally repulsive. Then, for given values of U/t and V/t, the appropriate values of V_x and a_s can be found, which in turn determines the values of t_{nnn}/t, V_{nnn}/t, and T/t.

Let us remark that one can, in principle, employ a transverse harmonic confinement of the boson gas [32] to change the relative values of the parameters of dipolar interactions. We have found that while it does provide more control over the values of T/t, ultimately, they have a magnitude similar to what we obtain solely with V_{opt}, and so we refrain from including that method in our considerations.

We denote the values of V and U restricted to only contact (dipolar) interactions as V_c (V_d) and U_c (U_d). In the most common parameter range used in this paper, V/U is of the order of 1. For the optical lattice that we consider (Appendix A), both V_c/U_c and V_d/U_d are smaller than 10^{-1} (see the inset in Fig. 1). Consequently, for a given positive value of d, the value of a_s has to be negative in order to lower the value of U to achieve the desired V/U.

We now take a closer look at how changes in the dipolar interaction strength influence the validity of using (1) for a fixed phase diagram point (U/t, V/t). V_d and U_d increase linearly with d, and so must $|a_s|$ if we want to maintain the desired ratio of V/U. To keep V/t (which is approximately V_d/t) and U/t unchanged, the lattice must be made shallower (as t depends solely on V_x). Since the tight-binding approximation is no longer correct for shallow lattices, this provides an effective upper limit for t, which gets stricter as d increases. The maximum value of d we consider in this paper is 0.1, which corresponds to V_x being roughly equal to $2.5E_R$ for the exemplary values of $U/t = 2$ and $V/t = 1.5$ (see Fig. 1, where we also plot the resulting values of V_{nnn}/t, T/t, and t_{nnn}/t).

To give an example of the magnitude of d for real atoms and molecules, we first assume the lattice constant is $a = 532$ nm. Single atoms have weak dipole moments (for ^{52}Cr, $d \approx 9.7\times10^{-4}$; for ^{168}Er, $d \approx 4.3\times10^{-3}$; and for ^{164}Dy, $d \approx 8.5\times10^{-3}$) [29,30,40]. The values for molecules can be a few orders of magnitude greater (for $^{168}\text{Er}_2$, $d \approx 0.1$) [4]. It is worth noting that multiple experimental methods of decreasing

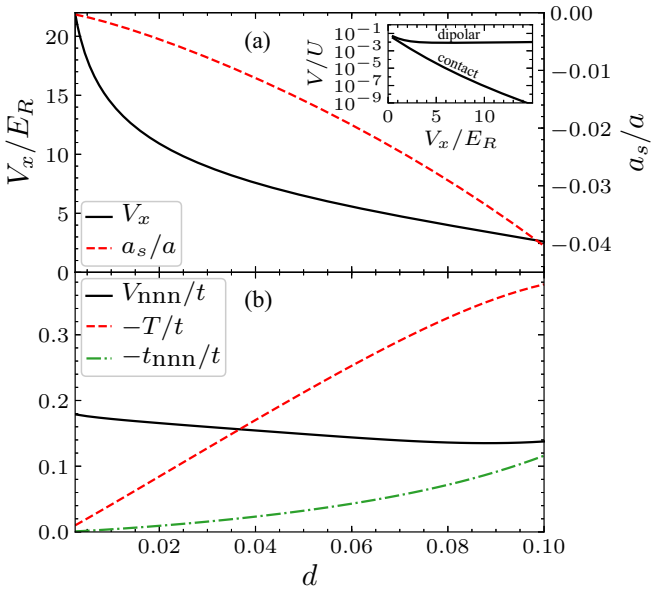

FIG. 1. (a) Values of V_x and a_s/a necessary to get $U/t = 2$ and $V/t = 1.5$ for different values of d. (b) Values of parameters in Hamiltonian (1) in such a case. The inset shows the values of V/U for dipolar-only and contact-only terms.

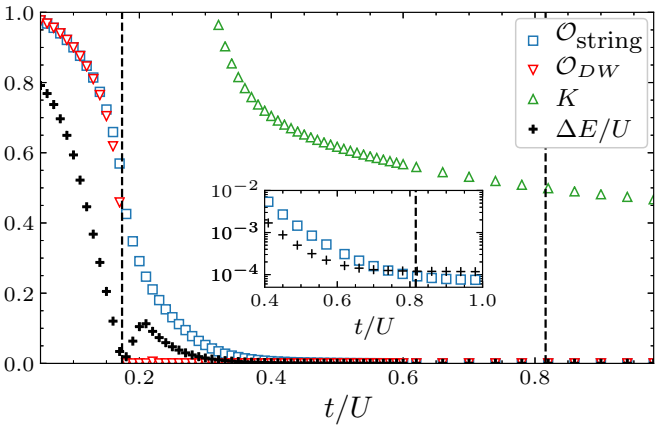

FIG. 2. The values of the string and DW order parameters, critical exponent K, and energy gap ΔE for $V/U = 3/4$, $d = 0.02$. The positions of black dashed vertical lines correspond to the critical values of t/U for DW-HI and HI-SF transitions ($t_c^{\text{DW-HI}}/U \approx 0.175$ and $t_c^{\text{HI-SF}} \approx 0.82$). The inset shows a logarithmic plot of $\mathcal{O}_{\text{string}}$ and ΔE near the HI-SF transition.

a in optical lattices [which would increase d; see Eq. (5)] by a factor of 2 or 3 (with the prospect for a larger value) have been developed and tested [51–54].

III. THE PHASE TRANSITIONS AT $\rho = 1$

The full phase diagram calculated numerically for the EBH model with t, U, and V as the only parameters and a unit mean density $\rho = 1$ has been studied in detail already [24,25], and here we will only briefly sum up the possible phases observed in the $(V/t, U/t)$ plane. For large values of t, the system is in the SF phase, whereas large values of U/t with small V/t drive the system into the MI. Large enough values of V/t for a sufficient U/t put the system in the DW phase. The HI is present on the phase diagram in between the three previously mentioned phases, that is, for intermediate values of both V/t and U/t.

In this section we will calculate how the locations of the transitions between these phases change for the Hamiltonian (1), depending on dipolar interaction strength d. We will not, however, recover a full phase diagram, and instead, we focus on two lines, given by the constraints $V/U = 0.75$ and $U/t = 3$. The first of these values is chosen because it covers three of the phases achievable in the EBH model (DW, HI, and SF) and has already been extensively analyzed [25,26], while the second one allows us to examine the MI phase (in addition to DW and HI, which are also present in that case).

In order to determine the boundaries between different phases, we define their characteristic properties: (1) for DW, $\mathcal{O}_{\text{DW}} \neq 0$, $\Delta E \neq 0$, (2) for MI, $\mathcal{O}_{\text{DW}} = 0$, $\mathcal{O}_{\text{string}} = 0$, $\Delta E \neq 0$, (3) for HI, $\mathcal{O}_{\text{DW}} = 0$, $\mathcal{O}_{\text{string}} \neq 0$, $\Delta E \neq 0$, and (4) for SF, $\mathcal{O}_{\text{DW}} = \mathcal{O}_{\text{string}} = 0$, $\Delta E = 0$. Order parameters are defined similarly to those in [24], $\mathcal{O}_p \equiv \lim_{r\to\infty} C_p$, for the following correlators:

$$C_{\text{SF}}(r) = \langle b_j^\dagger b_{j+r} \rangle , \tag{6}$$

$$C_{\text{DW}}(r) = (-1)^r \langle \delta n_j \delta n_{j+r} \rangle , \tag{7}$$

$$C_{\text{string}}(r) = \langle \delta n_j e^{i\pi \sum_{j\leqslant k\leqslant j+r} \delta n_k} \delta n_{j+r} \rangle , \tag{8}$$

where $\delta n_j = n_j - \rho$. The energy gap and its thermodynamic limit extrapolation are defined simply as $\Delta E(L) = E^{(1)}(L) - E^{(0)}(L)$ and $\Delta E = \lim_{L\to\infty} \Delta E(L)$, where $E^{(k)}(L)$ is the energy of the kth excited state in a lattice of length L ($k = 0$ is the ground state).

We will also be using the fact that for the superfluid phase it can be shown, using the Luttinger liquid theory, that the correlations in the system show power-law decay [55]:

$$C_{\text{SF}}(r) \sim r^{-K/2}. \tag{9}$$

A. $V/U = 0.75$ constraint

We present the results of our calculations for the model (1) obtained using the DMRG method described in Appendix B. For t/U close to zero the system is in the DW phase. As the value of t/U is increased, the first transition is a DW-HI transition at $t_c^{\text{DW-HI}}/U$. The transition location can be easily determined because for $t = t_c^{\text{DW-HI}}$ (1) the gap ΔE closes and (2) the order parameter $\mathcal{O}_{\text{DW}}$ vanishes (see Fig. 2, where the values of the order parameters are plotted for $d = 0.02$). ΔE is linear with respect to t/U on both sides of the transition, which allows us to easily determine where the gap closes. Additionally, the function $a[(t - t_c)/U]^{-b}$ can be fitted to the numerically computed $\mathcal{O}_{\text{DW}}$ near the transition point for $t/U < t_c^{\text{DW-HI}}/U$. The values of t_c/U obtained with these methods are in agreement with each other (with a difference of less than 5×10^{-3} for every value of d that was considered).

For even larger t, the consecutive transition occurs between the HI and SF phases, but the determination of its location, $t_c^{\text{HI-SF}}/U$, proves to be more difficult. As in the earlier case,

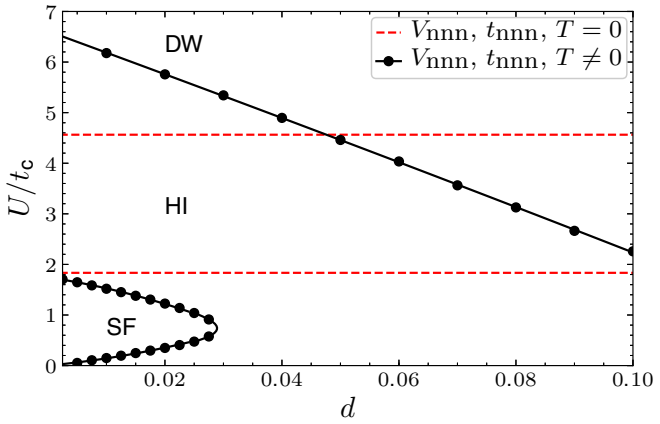

FIG. 3. Critical values of U/t for DW-HI and HI-SF transitions, $V/U = 3/4$ (black solid lines), and the same for a model with $V_{\rm nnn}$, $t_{\rm nnn}$, and T set to zero (red dashed lines).

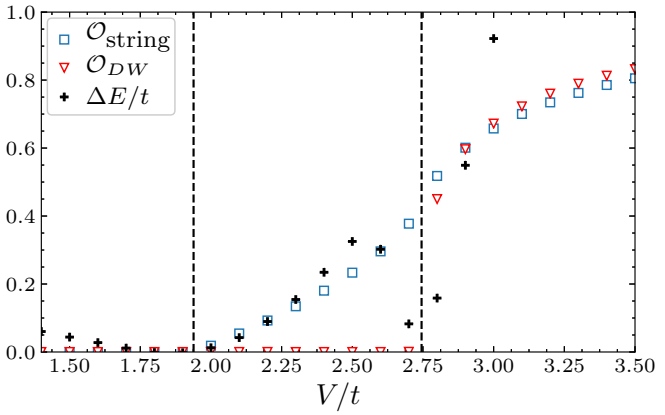

FIG. 4. The values of the order parameters (6), (7), and (8) for $U/t = 3$, $d = 0.09$. The positions of the black dashed vertical lines correspond to the critical values of V/t for DW-HI and HI-MI transitions ($V/t_c^{\rm HI-MI} \approx 1.94$ and $V/t_c^{\rm DW-HI} \approx 2.74$).

the energy gap closes, and the appropriate order parameter ($\mathcal{O}_{\rm string}$) goes to zero. However, the decay of both ΔE and $\mathcal{O}_{\rm string}$ features an exponential tail and does not provide a clear value of the transition point (see the inset of Fig. 2). In order to determine the correct value, we fit the correlations $C_{\rm SF}(r)$ for each L according to (9) and then extrapolate the obtained K to the $L \to \infty$ limit. It has been shown [56] that $K = 0.5$ for $\rho = 1$ at the transition between insulator and superfluid phases. That is the criterion we use here to determine $t_c^{\rm HI-SF}/U$.

The results of the analysis described above are shown in Fig. 3, where the dependence on the chosen d value for both DW-HI and HI-SF transitions is plotted as black solid lines. The results of similar calculations but with parameters $V_{\rm nnn}$, $t_{\rm nnn}$, and T set to zero are marked with the vertical red dashed lines. The U/t_c value for the DW-HI transition has a strong, linear dependence on d, and the transition point is moved considerably for both small and large values of d in the chosen interval ($0 < d \leqslant 0.1$). The situation is different for the HI-SF transition; while for values of d close to zero U/t_c is almost the same as for an ordinary EBH, the SF phase disappears completely around $d = 0.03$. What can also be seen for the intermediate values of d is that for small U/t_c another transition appears; in simulations we see the reemergence of the HI phase, indicated by a rise in $\mathcal{O}_{\rm string}$, ΔE, and K (the transition point is once again pinpointed by the equation $K = 0.5$). The striking substantial difference between the two models indicates that real care has to be taken when applying the tight-binding approximate Hamiltonian to a given physical system.

B. $U/t = 3$ constraint

In this case, two transitions exist between three insulating phases: DW-HI and HI-MI. The method of locating the HI-DW transition is the same as in Sec. III A (the corresponding plot of order parameters for $U/t = 3$ and $d = 0.09$ is shown in Fig. 4). For the HI-MI transition a different approach must be undertaken, as ΔE does not have a linear dependence on t near the transition point. To determine V/t_c we find the minimum of ΔE with respect to V/t for each available L, and then we extrapolate it for $L \to \infty$ using a power function $aL^{-b} + V/t_c$ (see Fig. 5).

We plot the results in Fig. 6, comparing them with the results obtained for a pure EBH model, i.e., setting $V_{\rm nnn}$, $t_{\rm nnn}$, and T in (1) to zero. While the changes are not as drastic as for fixed $V/U = 0.75$, the HI phase gets narrower with respect to V/t as d increases.

IV. THE PHASE DIAGRAM FOR $d = 0.1$

In this section, we characterize the phase diagram without constraining the density of particles ρ while setting $V/U = 0.75$ and $d = 0.1$. The results for an ordinary EBH model, obtained mostly using quantum Monte Carlo methods, can be found in [15,25]. To this end we calculate the ground-state energies using DMRG with OBCs (for technical details see Appendix B) for ρ corresponding to each of the DW phases present in the system for vanishing tunnelings. It is easy to convince oneself that the DW phase requires a commensurate relation between the number of particles and number of sites. Restricting the calculation to next-nearest-neighbor interactions, the corresponding densities are $\rho_{\rm DW} = n_{\rm DW}/4$, where $n_{\rm DW} \geqslant 2$, $n_{\rm DW} \in \mathbb{Z}$. Repeating the same calculations

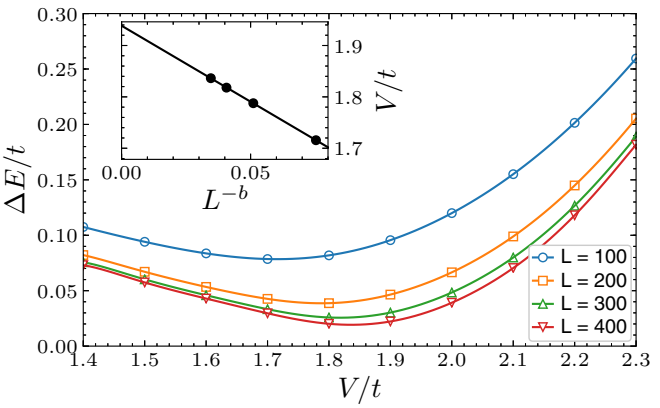

FIG. 5. The energy gap for different system sizes and $U/t = 3$, $d = 0.09$. The inset shows an extrapolation for $L \to \infty$, $b \approx 0.56151$.

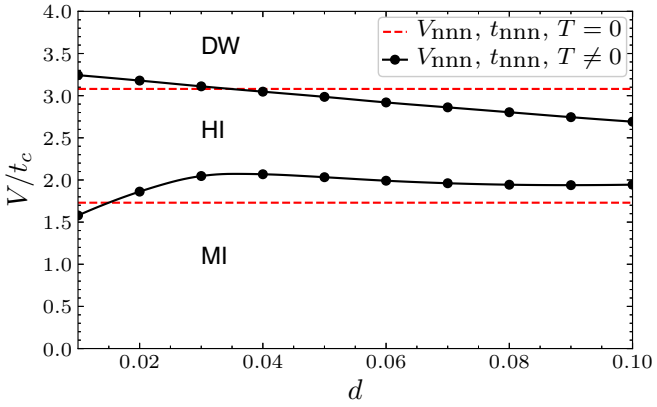

FIG. 6. Critical values of V/t for DW-HI and HI-SF transitions, $U/t = 3$ (black solid lines), and the same for a model with $V_{\rm nnn}$, $t_{\rm nnn}$, and T set to zero (red dashed lines).

with particles added or removed from the system allows us to obtain the chemical potential: $\mu(N,L) = \partial E(N,L)/\partial N$. We can then get the boundaries of DW phases as a discontinuity in $\mu(N,L)$ at $N_{\rm DW} = \rho_{\rm DW} L$. The lower boundary for the DW phase is then given by $\mu^- = \lim_{N\to N_{\rm DW}^+} \mu(N,L)$, while the upper one is given by $\mu^+ = \lim_{N\to N_{\rm DW}^-} \mu(N,L)$. By adjusting the system size we verify that systems with $L = 200$ are sufficiently large to properly determine the values of μ_L and μ_U; for most of the boundary $\mu^- = E(N,L) - E(N-1,L)$, and $\mu^+ = E(N+1,L) - E(N,L)$ [the only exception is the cusps at the rightmost edges of the DW lobes, where we take into account $E(N-2,L)$ and $E(N+2,L)$ and perform the quadratic interpolation]. The resulting phase diagram can be seen in Fig. 7. We remark that apart from the conventional $|0(2\rho)0(2\rho)0\cdots\rangle$ DW phases, with $\rho = \rho_{\rm DW}$, we observe $|0(2\rho-\frac{1}{2})0(2\rho+\frac{1}{2})\cdots\rangle$ phases for odd $n_{\rm DW}$ as an effect of introducing $V_{\rm nnn} n_i n_{i+2}$ coupling terms into the Hamiltonian. The corresponding DW regions are, fortunately, quite tiny, showing that for most parameters, the picture obtained within the EBH model is correct.

Apart from the abundant DW phases we observe either SF- or SS-like phases, as indicated by the power-law decay of the $C_{\rm SF}$ correlations (9). The difference between the two phases is a nonzero density wave order parameter value in the supersolid phase. The trivial SF phase is seen for $\rho < 1$; however, we observe the emergence of a pair superfluid (PSF) phase for large enough μ. We use the pair-tunneling correlation

$$C_p = \frac{1}{L}\sum_i \langle b_i^\dagger b_i^\dagger b_{i+1} b_{i+1}\rangle \tag{10}$$

as a measure of pair superfluidity (see Fig. 7). The phases marked SS and PSS (pair supersolid) in Fig. 7 differ from conventional supersolid phases in a simple EBH model, where $C_{\rm SF}(r)$ is always positive. $C_{\rm SF}(r)$ is negative for $r = 4n+2$, $n \in \mathbb{Z}$ in the SS phase [Fig. 8(a)] and for odd r in the PSS phase [Fig. 8(b)]. The other difference is that $C_p > 0$ in the PSS phase. We remark that both the PSS and PSF phases have been previously observed in numerical calculations for EBH Hamiltonians with density-dependent tunneling [32,57,58].

Next, we describe the last phase present in the phase diagram, which we call an incommensurate pair supersolid

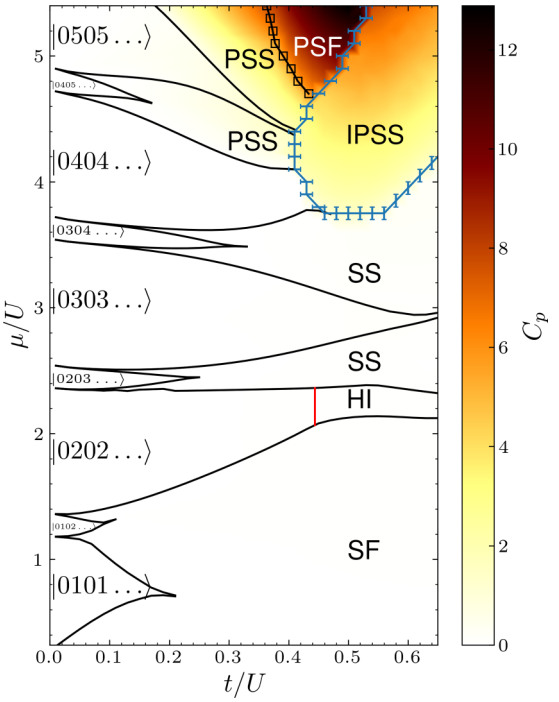

FIG. 7. The phases for the system for $d = 0.1$ at a fixed ratio $V/U = 0.75$. Black lines showing the boundaries of DW phases are the values of μ_+ and μ_- obtained from OBC DMRG ($L = 200$). The black squares come from sine-square deformation (SSD) DMRG (see Appendix C for details) for $L = 100$ and show the transition points between PSS and PSF (where $\mathcal{O}_{\rm DW}$ vanishes). Blue error bars mark the boundaries of the IPSS phase (and also SSD DMRG, $L = 100$). The value of pair-tunneling correlations C_p (10) is plotted as a color map with the scale shown on the right.

(IPSS). This phase is characterized by a finite, positive C_p and the structure factor

$$S(q) = \frac{1}{L^2}\sum_{j,k=1}^{L} \langle n_j n_k\rangle\, e^{-iq(j-k)}, \tag{11}$$

with a peak at $\pi/2 < q < \pi$, which is incommensurate with respect to lattice size and the particle density. In order to identify this phase, we use the sine-squared deformation (SSD) variant of the DMRG method which we describe in Appendix C.

In the IPSS we see periodic modulation of both density and density-density correlations [Fig. 9(a)] in the form of

$$\langle n_i\rangle = \rho_{\rm bulk} + \Delta\rho \sin(q_{\langle nn\rangle} i + \varphi_0), \tag{12}$$

$$\langle n_i n_{i+r}\rangle = C_1 + A_1 \sin(q_{\langle nn\rangle} r + \varphi_1) r^{-\alpha_1}, \tag{13}$$

where $q_{\langle nn\rangle}$ is the same wave-number value for which there is a peak in $S(q)$ [see Fig. 9(c)] The pair correlations also show the same modulation, while at the same time following a power-law decay [Fig. 9(b)],

$$\langle b_i^\dagger b_i^\dagger b_{i+r} b_{i+r}\rangle = [C_2 + A_2 \sin(q_{\langle nn\rangle} r + \varphi_2)] r^{-\alpha_2}. \tag{14}$$

Another modulation can be observed in $\langle b_i^\dagger b_{i+r}\rangle$; however, in this case the wave number differs from $q_{\langle nn\rangle}$, and the values

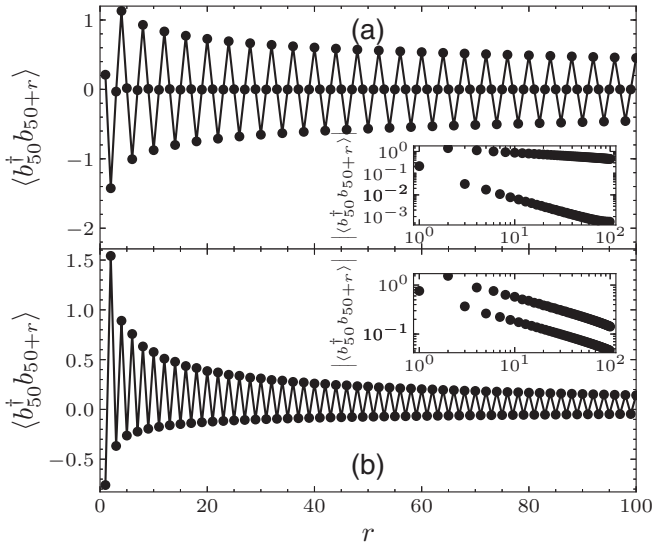

FIG. 8. OBC DMRG results of $\langle b_i^\dagger b_{i+r}\rangle$ correlations in the middle of an $L = 200$ lattice at (a) $\rho = 1.25$, $t/U = 0.59$ (SS phase) and (b) $\rho = 2.25$, $t/U = 0.37$ (PSS phase). Log-log plots of the same correlations are shown in the insets.

oscillate around zero [see Fig. 9(d)]:

$$\langle b_i^\dagger b_{i+r}\rangle = A_3 \sin(q_{\langle b^\dagger b\rangle} r + \varphi_3) r^{-\alpha_3}. \tag{15}$$

After combining the results for many different μ and t/U parameters, we can provide the relation between $q_{\langle b^\dagger b\rangle}$ and $q_{\langle nn\rangle}$ [see Fig. 10(a)]:

$$q_{\langle b^\dagger b\rangle} = \pi - 0.5 q_{\langle nn\rangle}. \tag{16}$$

We also note that is $q_{\langle nn\rangle}$ does not depend exclusively on ρ_{bulk} [which is the case in, e.g., underdoped $\rho = 0.5$ DW, where $q = 2\pi\rho$ [26]; see Fig. 10(b)].

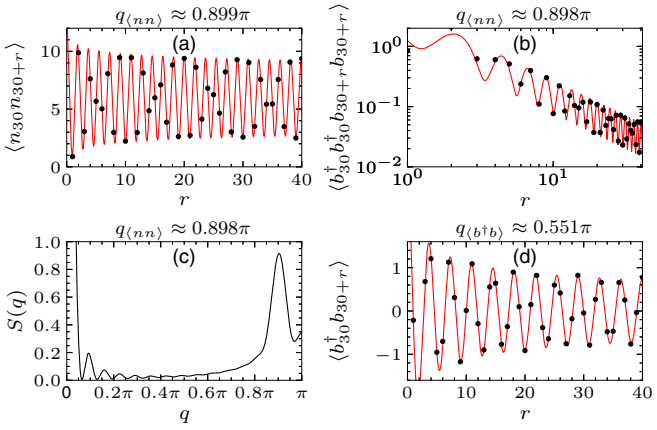

FIG. 9. Correlations and structure factor values obtained with SSD DMRG for the system in the IPSS phase ($L = 100$, $t/U = 0.48$, and $\mu = 3.7$). (a) Density correlations, (b) pair correlations, (c) structure factor (11), and (d) creation-annihilation correlations. For (a), (b), and (d), black points mark the numerical results, with red lines showing the fits of the functions in Eqs. (13) to (15). The value of the appropriate wave number q_α obtained from the fits [or from the position of the $S(q)$ peak in (c)] is written above each plot.

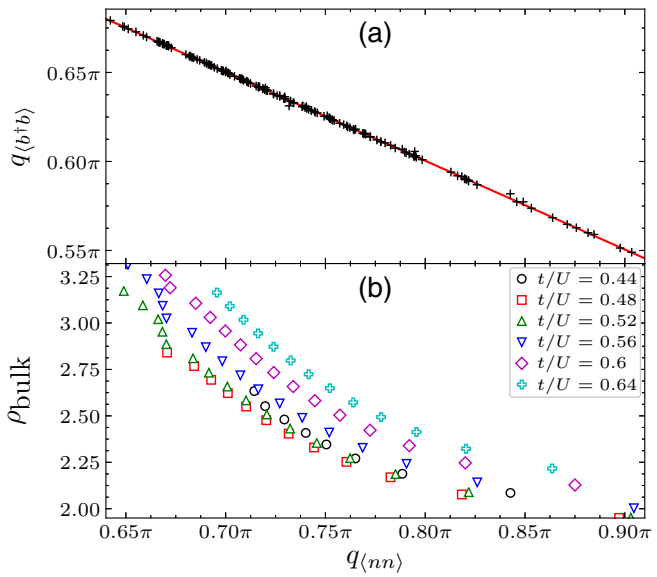

FIG. 10. The results of SSD DMRG for the IPSS phase. (a) The relation between $q_{\langle nn\rangle}$ and $q_{\langle b^\dagger b\rangle}$. The linear fit (red) is $q_{\langle b^\dagger b\rangle} = 0.9991(6)\pi - 0.4984(7) q_{\langle nn\rangle}$. (b) The relation between $q_{\langle nn\rangle}$ and ρ_{bulk} shown for different values of t/U.

V. CONCLUSIONS

In this paper we have presented an accurate Hamiltonian representation of a one-dimensional system of bosons in an optical lattice considering both the dipolar and contact interactions (the mutual strength of which may be balanced using the Feshbach resonance). We have employed the well-established DMRG method to measure the dependence of the phase transitions on often overlooked terms in the EBH model (most notably, the next-nearest-neighbor tunnelings and the density-dependent tunnelings). We have observed the suppression of the SF phase with rising dipolar interaction strength. In the case of fixed $\rho = 1$ we have also noted the stable presence of a nontrivial, highly nonlocally correlated HI phase throughout the considered parameters range, which is even more pronounced for realistic, low values of dipolar interactions. This robustness can be traced back to the fact that HI is a symmetry-protected topological state [59].

For greater dipolar interaction strength and higher densities we have observed interesting pair-correlated phases. Among those, we put a particular emphasis on characterizing a novel incommensurate pair superfluid phase, whose distinctive feature is an incommensurate density wave order. That phase is not present either in the standard EBH model or for large dipole-dipole interactions in small-diagonalization studies. We have also noticed a particular relation between wave numbers characterizing different correlations measured in this phase (16) which may provide some insight into how to construct an appropriate theoretical description. Rigorous theoretical treatment of the IPSS is, however, beyond the scope of this paper.

ACKNOWLEDGMENTS

This work was realized under National Science Centre (Poland) Projects No. 2015/19/B/ST2/01028 (K.B.), No.

2016/23/D/ST2/00721 (M.Ł.), and No. 2016/21/B/ST2/01086 (J.Z.). It was also supported in part by PL-Grid Infrastructure as well as by the EU H2020 Future and Emerging Technologies project QUIC (Grant No. 641122).

APPENDIX A: THE DETERMINATION OF HAMILTONIAN PARAMETERS

The values of the parameters in model (1) have been calculated numerically using Wannier function representation for a periodic boundary system with a standard optical lattice potential $V_{\rm opt}(\mathbf{r})$. In the numerical calculations described below we assume the lattice is in the form of a cube with N^3 sites, so that the total volume $\Omega = (Na)^3$, where $a = \pi/k_L$ is the lattice constant.

Bloch functions of the form

$$\phi_{\mathbf{k}}(\mathbf{r}) = e^{i\mathbf{k}\cdot\mathbf{r}} u_k(\mathbf{r}), \tag{A1}$$

where $u_k(\mathbf{r})$ is a function with the same periodicity as the lattice potential, are calculated for the noninteracting Hamiltonian, $H_{\rm NI} = \frac{-\hbar^2\nabla^2}{2m} + V_{\rm opt}(\mathbf{r})$, as the lowest-energy eigenvectors of the Schrödinger equation:

$$H_{\rm NI}\phi_{\mathbf{k}}(\mathbf{r}) = E_k\phi_{\mathbf{k}}(\mathbf{r}). \tag{A2}$$

Wannier functions can be calculated in the usual way [41] from the Bloch functions:

$$w_n(\mathbf{r}) = \frac{1}{\sqrt{N^3}} \sum_{\mathbf{k}\in \rm BZ} \phi_{\mathbf{k}}(\mathbf{r}) e^{-ik_x an}, \tag{A3}$$

where $\phi_{\mathbf{k}}(0)$ is real and positive, n is the number of the lattice site in the x direction (we assume $y = z = 0$), and the summation is done over $\mathbf{k} = (k_x, k_y, k_z)$ from the first Brillouin zone.

Substituting field operators of the form $\phi(\mathbf{r}) = \sum_i w_i(\mathbf{r}) b_i$ in (2), we get

$$\begin{aligned} t &= t_{i(i+1),} \\ t_{\rm nnn} &= t_{i(i+2),} \\ U &= V_{iiii}, \\ V &= V_{i(i+1)i(i+1)} + V_{i(i+1)(i+1)i}, \\ V_{\rm nnn} &= V_{i(i+2)i(i+2)} + V_{i(i+2)(i+2)i}, \\ T &= -0.5[V_{ii(i+1)i} + V_{iii(i+1)}], \end{aligned} \tag{A4}$$

with

$$t_{ij} = -\int_\Omega d\mathbf{r} w_i^*(\mathbf{r}) H_{\rm NI}\, w_j(\mathbf{r}), \tag{A5}$$

$$\begin{aligned} V_{ijkl} = &\int_\Omega d\mathbf{r_1} d\mathbf{r_2} w_i^*(\mathbf{r_1}) w_j^*(\mathbf{r_2}) \\ &\times V(\mathbf{r_1} - \mathbf{r_2}) w_k(\mathbf{r_1}) w_l(\mathbf{r_2}). \end{aligned} \tag{A6}$$

Integral (A5) is straightforward to calculate using (A2) and (A3). In order to calculate (A6), we use periodic extension of the interaction potential:

$$V(\mathbf{r}) = \frac{1}{\Omega} \sum_{\mathbf{k}} \widetilde{V}(\mathbf{k}) e^{i\mathbf{k}\cdot\mathbf{r}}, \tag{A7}$$

where $\mathbf{k} = \frac{2\pi}{Na}(n_1, n_2, n_3)$, $n_i \in \mathbb{N}$, and $\widetilde{V}(\mathbf{k}) = \widetilde{V}_c(\mathbf{k}) + \widetilde{V}_d(\mathbf{k})$ is the sum of the Fourier transforms of the contact and dipolar interaction potentials (3):

$$\widetilde{V}_c(\mathbf{k}) = \frac{4\pi\hbar^2 a_s}{m}, \quad \widetilde{V}_d(\mathbf{k}) = C_{dd}(\cos^2\gamma - 1/3), \tag{A8}$$

where γ is the angle between the direction of polarization and $\mathbf{k}$. For convenience, we group the Wannier functions with the same arguments $w_{ij}(\mathbf{r}) = w_i^*(\mathbf{r}) w_j(\mathbf{r})$:

$$\begin{aligned} V_{ijkl} &= \int_\Omega d\mathbf{r_1} w_{ik}(\mathbf{r_1}) \int_\Omega d\mathbf{r_2} V(\mathbf{r_1} - \mathbf{r_2}) w_{jl}(\mathbf{r_2}) \\ &= \int_\Omega d\mathbf{r_1} w_{ik}(\mathbf{r_1}) (V * w_{jl})(\mathbf{r_1}) \\ &= \frac{1}{\Omega} \int_\Omega d\mathbf{r_1} w_{ik}(\mathbf{r_1}) \sum_{\mathbf{k_2}} \widetilde{(V * w_{jl})}(\mathbf{k_2}) e^{i\mathbf{k_2}\cdot\mathbf{r}}. \end{aligned} \tag{A9}$$

We use the convolution theorem for the Fourier series to obtain

$$\begin{aligned} V_{ijkl} &= \frac{1}{\Omega} \int_\Omega d\mathbf{r}\, w_{ik}(\mathbf{r}) \sum_{\mathbf{k_2}} \widetilde{V}(\mathbf{k_2}) \widetilde{w_{jl}}(\mathbf{k_2}) e^{i\mathbf{k_2}\cdot\mathbf{r}} \\ &= \frac{1}{\Omega^2} \int_\Omega d\mathbf{r} \sum_{\mathbf{k_1}} \widetilde{w_{ik}}(\mathbf{k_1}) e^{i\mathbf{k_1}\cdot\mathbf{r}} \sum_{\mathbf{k_2}} \widetilde{V}(\mathbf{k_2}) \widetilde{w_{jl}}(\mathbf{k_2}) e^{i\mathbf{k_2}\cdot\mathbf{r}} \\ &= \frac{1}{\Omega^2} \sum_{\mathbf{k_1},\mathbf{k_2}} \widetilde{w_{ik}}(\mathbf{k_1}) \widetilde{V}(\mathbf{k_2}) \widetilde{w_{jl}}(\mathbf{k_2}) \int_\Omega d\mathbf{r}\, e^{i(\mathbf{k_1}+\mathbf{k_2})\cdot\mathbf{r}} \\ &= \frac{1}{\Omega} \sum_{\mathbf{k}} \widetilde{w_{ik}}(-\mathbf{k}) \widetilde{V}(\mathbf{k}) \widetilde{w_{jl}}(\mathbf{k}). \end{aligned} \tag{A10}$$

APPENDIX B: DMRG PARAMETERS

All of the numerical calculations reported in this paper were done using density-matrix renormalization group (DMRG) implementation found in the ITENSOR library [23]. For most of the work OBCs were used, with sizes from $L = 100$ to $L = 400$ and a maximum bond dimension $\chi = 600$. The cutoff ϵ was set to 10^{-12} [ϵ determines the number of singular values discarded after each singular-value decomposition step in the ITENSOR algorithm: $(\sum_{n\in\text{discarded}} \lambda_n^2)/(\sum_n \lambda_n^2) < \epsilon$]. In Sec. III, we limit the maximum number of particles on each lattice site $N_{\rm cut}$ to 5, while for the OBCs and the SSD DMRG used in Sec. IV the number is, respectively, up to 10 and 12.

Unless stated otherwise, a boundary term equal to $2\rho(n_1 V + n_2 V_{\rm nnn} + n_L V_{\rm nnn})$ was added to break the degeneracy of the DW state (the added term simulates a situation where we have four additional sites at the boundaries, with fixed $n_{-1} = 0$, $n_0 = 2\rho$, $n_{L+1} = 0$, and $n_{L+2} = 2\rho$, as expected in one of the DW ground states). Another motivation for adding these terms is to remove excitations on the edges in the HI phase.

APPENDIX C: THE DESCRIPTION OF SINE-SQUARED DEFORMATION DMRG

Some of the calculations (determination of boundaries of the IPSS phase in Sec. IV) were performed using a smooth-boundary DMRG method, referred to as a sine-squared deformation (SSD) DMRG. In this approach the Hamiltonian

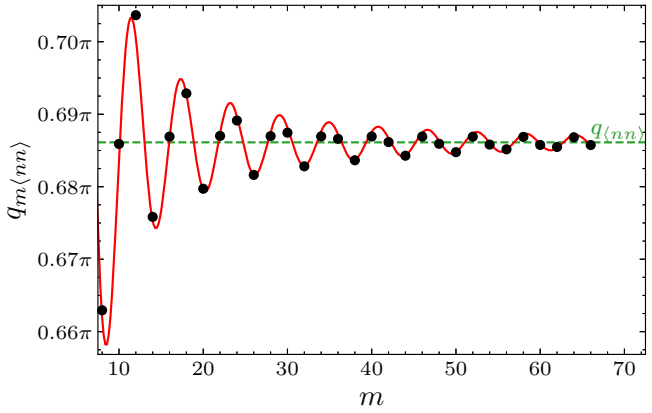

FIG. 11. Position of the peak in $S(q)$ (11) computed using m middle sites (black points). The red solid line shows a fit of the form $C + A\,m^{-B}\cos(Km+\phi)$. Here $K \approx 0.342\pi$, which is roughly half of $q_{\langle nn\rangle} = C \approx 0.686\pi$ (shown as a green dashed line). At most 2/3 of all lattice sites have been considered. Data are calculated for $\mu/U = 5.2$, $t/U = 0.6$, $L = 100$, and $N_{\text{cut}} = 12$. The damped oscillation amplitude $S(q)$ position is approximately an order of magnitude smaller than the FWHM of the $S(q)$ function, which for maximal m is $\approx 0.03\pi$.

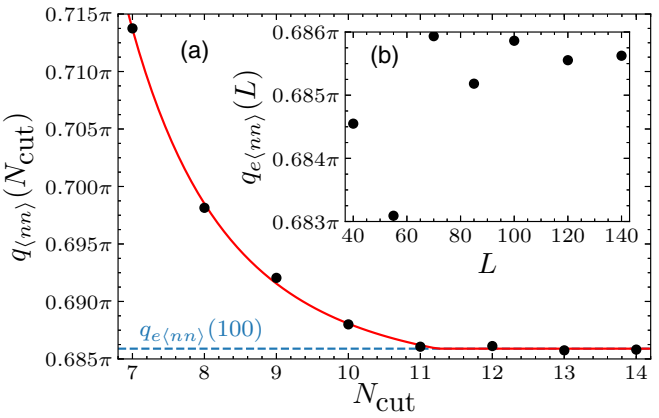

FIG. 12. (a) Position of the $S(q)$ peak $q_{\langle nn\rangle}$ (see Fig. 11) calculated for different values of maximum particles per site cutoff N_{cut} for $L = 100$. The red solid line shows a power-law decay to a constant value $q_{e\langle nn\rangle}$ (reached for a finite N_{cut}, here approximately 11.24; shown as a blue dashed line). (b) Values of $q_{e\langle nn\rangle}$ calculated for different system sizes L. Data for (a) and (b) were calculated for $\mu/U = 5.2$ and $t/U = 0.6$. The position of the $S(q)$ peak for $N_{\text{cut}} \geqslant 10$ $S(q)$ and for $L \geqslant 40$ changes by at least one order of magnitude less than the corresponding FWHM.

is rescaled using a sine-squared deformation [60]: $H_{\text{SDD}} = \sum_{j=0}^{2}\sum_{i=1}^{L-j} f_{i,j} H_{i,i+j}$, where

$$f_{i,j} = \sin^2\left[\frac{\pi}{L}\left(i + \frac{j-1}{2}\right)\right], \tag{C1}$$

with $H_{i,i+j}$ acting only on sites i and $i+j$ and $H_{i,i} \equiv H_i$ acting only on a single site, i. We also add a chemical potential term to the Hamiltonian, so that now $H_i = (U/2)n_i(n_i-1) - \mu n_i$.

In contrast to regular DMRG methods, the density of the gas of particles (as measured in the middle part of the lattice) is not fixed by the number of particles N used in the simulation, but rather by the value of μ. An excess (or a deficit) of particles stemming from the choice of N is taken care of by placing extra particles (vacancies) close to the system boundary, where the coefficient $f_{i,j}$ takes a minimal value. This makes the edges act as an effective bath for the particles (holes) in the middle of the lattice. Because of that, in determination of the physical quantities, we consider only 40% of the sites in the middle of the lattice, unless stated otherwise.

We pick N such that it does not differ much from $L\rho_{\text{bulk}}$, the number compatible with the bulk density. This ensures that fewer particles are displaced to (from) the edges, which minimizes the undesired boundary effects on the computed expectation values in the middle of the system.

In order to find the values of wave numbers $q_{\langle b^\dagger b\rangle}$ and $q_{\langle nn\rangle}$ [plotted in Fig. 10(a)] we look at the position of the peak of $S(q)$ (11) (or an analogical quantity for $\langle b^\dagger b\rangle$ correlations). To remove the boundary effects from our analysis, we consider only m lattice sites in the middle when calculating the structure factor. Depending on m, the position of the peak $q_{m\langle nn\rangle}$ oscillates with decreasing amplitude (see Fig. 11) around a value $q_{\langle nn\rangle}$, which is the one used in the main text.

As the mean densities in the IPSS phase in our calculations are quite high [with sites filled by more than six particles; Fig. 10(b)], we calculated how the cutoff on maximum particles per site N_{cut} in DMRG calculations affects the obtained value of $q_{\langle nn\rangle}$ [Fig. 12(a)], taking as an example values of $\mu/U = 5.2$ and $t/U = 0.6$, corresponding to $\rho_{\text{bulk}} \approx 3.1$. For each system size L we define $q_{e\langle nn\rangle}(L) = \lim_{N_{\text{cut}}\to\infty} q_{\langle nn\rangle}(N_{\text{cut}})$ and plot its value in Fig. 12(b). We determine that $N_{\text{cut}} = 12$ and $L = 100$ are enough to get converged values of wave numbers, and these parameters were used for SSD DMRG calculations.

[1] D. Jaksch, C. Bruder, J. I. Cirac, C. W. Gardiner, and P. Zoller, Phys. Rev. Lett. **81**, 3108 (1998).
[2] M. Greiner, O. Mandel, T. Esslinger, T. W. Hänsch, and I. Bloch, Nature (London) **415**, 39 (2002).
[3] C. Chin, R. Grimm, P. Julienne, and E. Tiesinga, Rev. Mod. Phys. **82**, 1225 (2010).
[4] A. Frisch, M. Mark, K. Aikawa, S. Baier, R. Grimm, A. Petrov, S. Kotochigova, G. Quéméner, M. Lepers, O. Dulieu, and F. Ferlaino, Phys. Rev. Lett. **115**, 203201 (2015).
[5] E. G. Dalla Torre, E. Berg, and E. Altman, Phys. Rev. Lett. **97**, 260401 (2006).
[6] S. Sinha and L. Santos, Phys. Rev. Lett. **99**, 140406 (2007).
[7] T. Lahaye, C. Menotti, L. Santos, M. Lewenstein, and T. Pfau, Rep. Prog. Phys. **72**, 126401 (2009).
[8] J. Ruhman, E. G. Dalla Torre, S. D. Huber, and E. Altman, Phys. Rev. B **85**, 125121 (2012).
[9] M. A. Baranov, M. Dalmonte, G. Pupillo, and P. Zoller, Chem. Rev. **112**, 5012 (2012).

[10] M. Wall and L. Carr, New J. Phys. **15**, 123005 (2013).
[11] A. Gallemí, M. Guilleumas, R. Mayol, and A. Sanpera, Phys. Rev. A **88**, 063645 (2013).
[12] S. Gammelmark and N. T. Zinner, Phys. Rev. B **88**, 245135 (2013).
[13] O. Dutta, M. Gajda, P. Hauke, M. Lewenstein, D.-S. Lühmann, B. A. Malomed, T. Sowiński, and J. Zakrzewski, Rep. Prog. Phys. **78**, 066001 (2015).
[14] A. Gallemí, G. Queraltó, M. Guilleumas, R. Mayol, and A. Sanpera, Phys. Rev. A **94**, 063626 (2016).
[15] K. Kawaki, Y. Kuno, and I. Ichinose, Phys. Rev. B **95**, 195101 (2017).
[16] F. Cartarius, A. Minguzzi, and G. Morigi, Phys. Rev. A **95**, 063603 (2017).
[17] S. Baier, M. J. Mark, D. Petter, K. Aikawa, L. Chomaz, Z. Cai, M. Baranov, P. Zoller, and F. Ferlaino, Science **352**, 201 (2016).
[18] D. Delande and J. Zakrzewski, Phys. Rev. Lett. **102**, 085301 (2009).
[19] A. L. Gaunt, T. F. Schmidutz, I. Gotlibovych, R. P. Smith, and Z. Hadzibabic, Phys. Rev. Lett. **110**, 200406 (2013).
[20] M. Łącki, H. Pichler, A. Sterdyniak, A. Lyras, V. E. Lembessis, O. Al-Dossary, J. C. Budich, and P. Zoller, Phys. Rev. A **93**, 013604 (2016).
[21] H. Kim, G. Zhu, J. V. Porto, and M. Hafezi, arXiv:1805.01483.
[22] U. Schollwöck, Ann. Phys. (NY) **326**, 96 (2011).
[23] ITENSOR library, http://itensor.org.
[24] D. Rossini and R. Fazio, New J. Phys. **14**, 065012 (2012).
[25] G. G. Batrouni, V. G. Rousseau, R. T. Scalettar, and B. Grémaud, Phys. Rev. B **90**, 205123 (2014).
[26] B. Grémaud and G. G. Batrouni, Phys. Rev. B **93**, 035108 (2016).
[27] E. Wikberg, J. Larson, E. J. Bergholtz, and A. Karlhede, Phys. Rev. A **85**, 033607 (2012).
[28] T. Đurić, K. Biedroń, and J. Zakrzewski, Phys. Rev. B **95**, 085102 (2017).
[29] M. Lu, N. Q. Burdick, S. H. Youn, and B. L. Lev, Phys. Rev. Lett. **107**, 190401 (2011).
[30] K. Aikawa, A. Frisch, M. Mark, S. Baier, A. Rietzler, R. Grimm, and F. Ferlaino, Phys. Rev. Lett. **108**, 210401 (2012).
[31] A. Chotia, B. Neyenhuis, S. A. Moses, B. Yan, J. P. Covey, M. Foss-Feig, A. M. Rey, D. S. Jin, and J. Ye, Phys. Rev. Lett. **108**, 080405 (2012).
[32] T. Sowiński, O. Dutta, P. Hauke, L. Tagliacozzo, and M. Lewenstein, Phys. Rev. Lett. **108**, 115301 (2012).
[33] S. A. Moses, J. P. Covey, M. T. Miecnikowski, B. Yan, B. Gadway, J. Ye, and D. S. Jin, Science **350**, 659 (2015).
[34] S. A. Moses, J. P. Covey, M. T. Miecnikowski, D. S. Jin, and J. Ye, Nat. Phys. **13**, 13 (2017).
[35] P. Sengupta, L. P. Pryadko, F. Alet, M. Troyer, and G. Schmid, Phys. Rev. Lett. **94**, 207202 (2005).
[36] G. G. Batrouni, F. Hébert, and R. T. Scalettar, Phys. Rev. Lett. **97**, 087209 (2006).
[37] T. Mishra, R. V. Pai, S. Ramanan, M. S. Luthra, and B. P. Das, Phys. Rev. A **80**, 043614 (2009).
[38] B. Capogrosso-Sansone, C. Trefzger, M. Lewenstein, P. Zoller, and G. Pupillo, Phys. Rev. Lett. **104**, 125301 (2010).
[39] M. P. Zaletel, S. A. Parameswaran, A. Rüegg, and E. Altman, Phys. Rev. B **89**, 155142 (2014).
[40] M. Lewenstein, A. Sanpera, and V. Ahufinger, *Ultracold Atoms in Optical Lattices: Simulating Quantum Many-Body Systems* (Oxford University Press, Oxford, 2012).
[41] W. Kohn, Phys. Rev. **115**, 809 (1959).
[42] M. Łącki and J. Zakrzewski, Phys. Rev. Lett. **110**, 065301 (2013).
[43] H. Pichler, J. Schachenmayer, A. J. Daley, and P. Zoller, Phys. Rev. A **87**, 033606 (2013).
[44] M. Maik, P. Hauke, O. Dutta, M. Lewenstein, and J. Zakrzewski, New J. Phys. **15**, 113041 (2013).
[45] D.-S. Lühmann, O. Jürgensen, and K. Sengstock, New J. Phys. **14**, 033021 (2012).
[46] U. Bissbort, F. Deuretzbacher, and W. Hofstetter, Phys. Rev. A **86**, 023617 (2012).
[47] M. Łącki, D. Delande, and J. Zakrzewski, New J. Phys. **15**, 013062 (2013).
[48] C. Kollath, G. Roux, G. Biroli, and A. M. Läuchli, J. Stat. Mech. (2010) P08011.
[49] S. Trotzky, Y.-A. Chen, A. Flesch, I. P. McCulloch, U. Schollwöck, J. Eisert, and I. Bloch, Nat. Phys. **8**, 325 (2012).
[50] K. Góral, L. Santos, and M. Lewenstein, Phys. Rev. Lett. **88**, 170406 (2002).
[51] T. Salger, C. Geckeler, S. Kling, and M. Weitz, Phys. Rev. Lett. **99**, 190405 (2007).
[52] W. Yi, A. J. Daley, G. Pupillo, and P. Zoller, New J. Phys. **10**, 073015 (2008).
[53] Q. Sun, J. Evers, M. Kiffner, and M. S. Zubairy, Phys. Rev. A **83**, 053412 (2011).
[54] S. Nascimbene, N. Goldman, N. R. Cooper, and J. Dalibard, Phys. Rev. Lett. **115**, 140401 (2015).
[55] T. Giamarchi, *Quantum Physics in One Dimension*, International Series of Monographs on Physics, Vol. 121 (Oxford University Press, Oxford, 2004).
[56] T. D. Kühner, S. R. White, and H. Monien, Phys. Rev. B **61**, 12474 (2000).
[57] H.-C. Jiang, L. Fu, and C. Xu, Phys. Rev. B **86**, 045129 (2012).
[58] A. Rapp, X. Deng, and L. Santos, Phys. Rev. Lett. **109**, 203005 (2012).
[59] K. Wierschem and P. Sengupta, Mod. Phys. Lett. B **28**, 1430017 (2014).
[60] T. Hikihara and T. Nishino, Phys. Rev. B **83**, 060414 (2011).